

Reconfigurable nanoscale spin wave majority gate with frequency-division multiplexing

Giacomo Talmelli,^{1,2} Thibaut Devolder,³ Nick Träger,⁴ Johannes Förster,⁴ Sebastian Wintz,^{4,5} Markus Weigand,^{4,6} Hermann Stoll,⁴ Marc Heyns,^{1,2} Gisela Schütz,⁴ Iuliana P. Radu,¹ Joachim Gräfe,⁴ Florin Ciubotaru,¹ and Christoph Adelmann^{1,*}

¹*IMEC, 3001 Leuven, Belgium*

²*KU Leuven, Departement Materiaalkunde, SIEM, 3001 Leuven, Belgium*

³*Centre de Nanosciences et de Nanotechnologies, CNRS,*

Université Paris-Sud and Université Paris-Saclay, 91120 Palaiseau, France

⁴*Max-Planck-Institut für Intelligente Systeme, 70569 Stuttgart, Germany*

⁵*Paul Scherrer Institut, 5232 Villigen, Switzerland*

⁶*Helmholtz-Zentrum Dresden-Rossendorf, 01328 Dresden, Germany*

Abstract

Spin waves are excitations in ferromagnetic media that have been proposed as information carriers in spintronic devices with potentially much lower operation power than conventional charge-based electronics. The wave nature of spin waves can be exploited to design majority gates by coding information in their phase and using interference for computation. However, a scalable spin wave majority gate design that can be co-integrated alongside conventional Si-based electronics is still lacking. Here, we demonstrate a reconfigurable nanoscale inline spin wave majority gate with ultra-small footprint, frequency-division multiplexing, and fan-out. Time-resolved imaging of the magnetisation dynamics by scanning transmission x-ray microscopy reveals the operation mode of the device and validates the full logic majority truth table. All-electrical spin wave spectroscopy further demonstrates spin wave majority gates with sub- μm dimensions, sub- μm spin wave wavelengths, and reconfigurable input and output ports. We also show that interference-based computation allows for frequency-division multiplexing as well as the computation of different logic functions in the same device. Such devices can thus form the foundation of a future spin-wave-based superscalar vector computing platform.

Why spin wave majority gates? Spin waves are dynamic excitations in ferromagnetic media with characteristic wavelengths from nm to μm scales and frequencies from GHz to THz. Due to their low intrinsic energy, they have received increasing interest as information carriers in magnonic computation schemes [1, 2] operating potentially at much lower power than current charge-based complementary metal-oxide-semiconductor (CMOS) technology. Numerous fundamental building blocks [3, 4] for magnonic logic have been proposed and realised, including methods for spin wave routing [5–9], multiplexing [10, 11], signal regeneration [12], amplification [13, 14], and gating [15–19]. Spin waves are particularly suited for the realisation of compact interference-based majority gates with potentially large additional benefits in area scaling over CMOS [20–22]. In initial work, spin wave majority gates based on a trident design have been proposed [20, 23] and their basic functionality has been experimentally demonstrated for mm-size devices [24]. Such majority gates occupy areas of the order of $30 F^2$ with F the critical dimension of the device, which compares favourably with the $\sim 330 F^2$ required for majority gates implemented in CMOS [25], leading to potentially large area gains of spin wave technology. However, the trident design has severe drawbacks when miniaturised to the nanoscale, such as narrow operation windows, strong spin wave attenuation at the trident bends, and limited compatibility with conventional lithography processes. Moreover, the previous mm-scale experimental demonstration has relied on low-damping $\text{Y}_3\text{Fe}_5\text{O}_{12}$ (yttrium iron garnet, YIG), resulting in low spin wave group velocities below $1 \mu\text{m}/\text{ns}$ in nm-thin films, long spin wave lifetimes, and thus low computational throughput. In addition, the magnetic properties of YIG and thus the spin wave dispersion relation depend strongly on temperature in the relevant operation range, rendering the usage of YIG for actual wave-based spintronic devices impractical. By contrast, an ideal spin wave majority gate combines ultracompact size, scalability to nm dimensions, low temperature sensitivity, fast operation, possibility for fan-out, and a wide operation window with a flexible design that alleviates lithography constraints and lowers manufacturing cost.

Operation principle of the inline spin wave majority gate. The basic structure and the operation principle of our inline spin wave majority gate is depicted in Fig. 1a. Three input ports, P_1 , P_2 , and P_3 , as well as one or two output ports, O and O' , are placed at equally-spaced positions $n \times 2F$ on a spin wave waveguide [26], with $n = 1, 2, 3, 4$ and

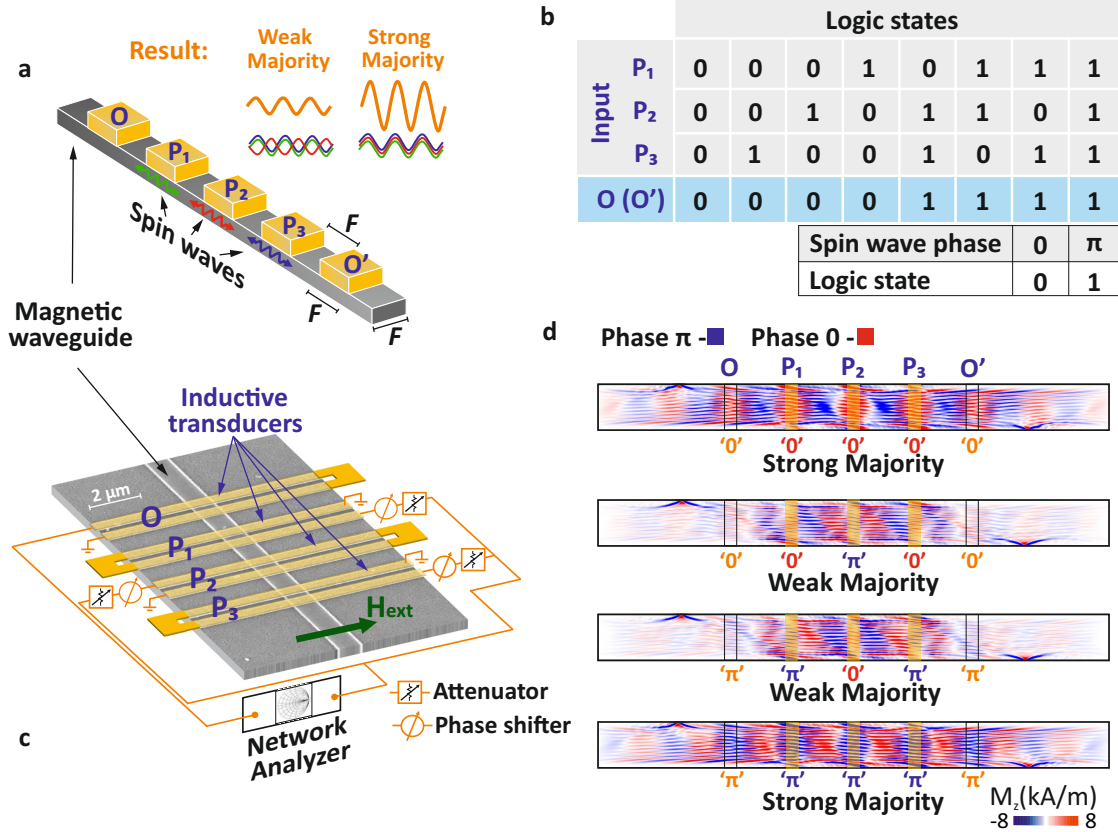


FIG. 1. **Device structure and operation principle of the inline spin wave majority gate.**

a) Schematic of an inline spin wave majority gate with three inputs (P_1 , P_2 , and P_3) and two outputs (O and O'), *i.e.* with a fan-out of two. **b)** Truth table of the majority function. **c)** Scanning-electron micrograph of a fabricated spin wave majority gate with a 850-nm-wide $\text{Co}_{40}\text{Fe}_{40}\text{B}_{20}$ waveguide, three input antennas, and one output antenna. **d)** Steady-state snapshot images (in phase with the logic 0 signal) of the out-of-plane magnetisation obtained by micromagnetic simulations during spin wave majority gate operation using spin wave modes confined in an 850-nm-wide $\text{Co}_{40}\text{Fe}_{40}\text{B}_{20}$ waveguide. Operation frequency 13.9 GHz, magnetic bias field $\mu_0 H_{ext} = 80$ mT.

F the characteristic dimension of the device that is (much) smaller than the spin wave attenuation length. For F^2 transducers at the ports, the inline spin wave majority gate occupies an ultrasmall area of $16 F^2$ ($20 F^2$ for a device with two output ports and thus a fan-out of two), much smaller than CMOS implementations and even significantly smaller than trident-based spin wave majority gate designs. Using microwave signals at the input ports, coherent spin waves of unit amplitude are launched at the three input ports and propagate in the waveguide. Binary logic signals are encoded in the phases of the individual

spin waves using phases of 0 and π as logic 0 and 1, respectively. Constructive or destructive interference leads then to an output wave with a phase that corresponds to the majority of the individual spin wave phases, $\text{MAJ}(\varphi_1, \varphi_2, \varphi_3)$, with MAJ being the ternary majority operator (Fig. 1b). The amplitude of the output wave can also give information whether weak or strong majority is obtained. The generalisation to majority gates with more than three inputs is straightforward.

To obtain a functionally complete set of logic gates, the spin wave majority gate must be complemented by another wave-based logic gate. Inverters (logic NOT) provide a highly appealing solution since their implementation in phase-coded wave-based computing corresponds to a simple phase shift by π . In contrast to CMOS technology, wave-based inverters do not need to be separate logic gates but can be integrated in the majority gate design. Physical implementations can be based on a spin wave delay line with a length of $(i - \frac{1}{2}) \times \lambda$, with $i = 1, 2, 3, \dots$ an integer and λ the spin wave wavelength, which can be *e.g.* realised by shifting input or output ports away from their equally-spaced positions. In addition, shifting the phase or reverting the polarity (signal *vs.* ground) of an input or output port can also be used to invert the logic signal. These implementations lead to little to no increase in device area, and, in the second case, to no additional restrictions on operating conditions.

Implementation. Miniaturising spin wave majority gates to nm dimensions allows for the usage of ferromagnetic waveguide materials with moderate Gilbert damping (and thus shorter spin wave attenuation lengths) than ultralow-damping single-crystal YIG that has been used for mm-size trident-based spin wave majority gate realisations [24]. YIG suffers from temperature-dependent low saturation magnetisation, low spin wave group velocities, and very long spin wave lifetimes [27], leading to low computation throughput. Moreover, single-crystal YIG cannot be integrated alongside conventional CMOS on Si wafers. By contrast, metallic ferromagnets such as CoFeB and permalloy ($\text{Ni}_{80}\text{Fe}_{20}$) with much larger saturation magnetisation and higher Curie temperature promise faster operation, lower temperature sensitivity, and are compatible with established semiconductor process technology. Our implementation will thus be based on $\text{Co}_{40}\text{Fe}_{40}\text{B}_{20}$ and permalloy waveguides with widths down to 850 nm (Fig. 1c). In such narrow waveguides, the mode patterns of confined spin waves deviate significantly from the plane waves employed in previous macroscopic spin wave majority gate implementations [24] due to the nonuniformity of the static magneti-

sation and the internal effective field in the commonly-used Damon-Eshbach configuration [34]. Micromagnetic simulations in Fig. 1d for 850-nm-wide $\text{Co}_{40}\text{Fe}_{40}\text{B}_{20}$ waveguides in the Damon-Eshbach geometry show the excitation of spin waves confined in the centre of the waveguide and modulated by backward-volume spin waves that are excited at the edges and propagate preferentially towards the centre. Yet, the simulations still demonstrate majority gate operation in such a device despite the rather complex mode patterns when the phase of the magnetisation precession at the output port is analysed. Animations of the full magnetisation dynamics for different sets of input phases can be found in the supplementary information.

Different approaches for spin wave transducers that couple spin wave and microwave signals have been reported in the literature [28–31]. In this work, we employ inductive microwave antennas [32] as both input and output ports because they combine high maturity and robustness with broadband excitation and detection of spin waves [33]. For all-electrical operation of spin wave majority gates, U-shaped antennas were used because of their low parasitic crosstalk. By contrast, spin wave majority gate imaging by time-resolved scanning transmission x-ray microscopy was performed using more compact single wire antennas. Details about the antenna design can be found in the supplementary information. In all experiments, the waveguides were magnetised transversally in the Damon-Eshbach configuration [34] using an external magnetic bias field. This configuration leads to spin waves with large group velocities (of the order of 5–10 $\mu\text{m}/\text{ns}$ for our $\text{Co}_{40}\text{Fe}_{40}\text{B}_{20}$ waveguides), which efficiently couple to the microwave antennas at the input and output ports.

Time-resolved imaging of spin-wave majority gate operation. The operation of the spin wave majority gate requires that the phases of the individual spin waves for a given logic level are matched at the port where the output signal is read. In general, this does not require that the phases of the microwave signals and the individual spin waves are matched *at the input ports*. In scaled circuits on a chip, however, accurate large phase shifts of the input microwave signals may be difficult to generate for individual inputs and it is thus desirable to use identical microwave signals for a given logic level at *all* input ports. This can be realised under “resonant” operation conditions when the interport distance $2F$ is equal to $N \times \lambda$ with $N = 1, 2, 3, \dots$ an integer and λ the spin wave wavelength. The spin wave phase then rotates by integer multiples of 2π during propagation from any of the three

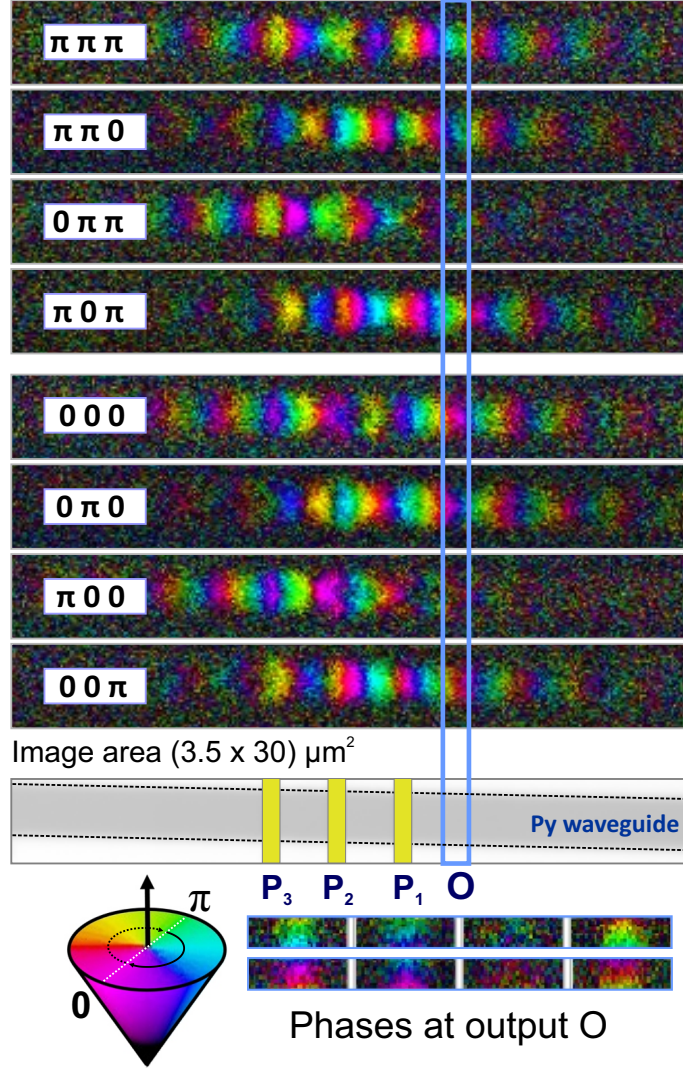


FIG. 2. **Visualisation of spin-wave majority gate operation.** Spatial phase distribution of the magnetisation dynamics in a spin wave majority gate (2.0- μm -wide permalloy waveguide, operation frequency 8.6 GHz, magnetic bias field $\mu_0 H_{\text{ext}} = 80$ mT) imaged by time-resolved scanning transmission x-ray microscopy for different sets of input phases. Detecting the spin wave phase at the output position O allows for the reconstruction of the truth table of the majority function.

input ports to the output port, leading to matched phases both at the individual inputs and the output.

The operation of an inline spin wave majority gate can be visualised by imaging the magnetisation dynamics in the waveguide by time-resolved scanning transmission x-ray microscopy. In these experiments, spin waves are excited in a 2.0- μm -wide permalloy waveguide by microwave currents in three input antennas P_1 , P_2 , and P_3 , each separated by a distance

of $2F = 2.5 \mu\text{m}$. Binary logical signals 0 and 1 are encoded as spin wave phases of 0 (reference) and π , respectively. The logical output signal is determined by extracting the phase of the resulting spin wave at position O , about $2.2 \mu\text{m}$ away from P_1 , from the measured time dependence of the magnetisation dynamics. An operation frequency of 8.6 GHz and an external magnetic bias field of $\mu_0 H_{\text{ext}} = 80 \text{ mT}$ lead to a measured spin wave wavelength of $2.4 \mu\text{m}$, which is very close to the interport distance. Thus, resonant operation conditions are approximately realised with $N = 1$. The phase maps of the magnetisation dynamics at position O in Fig. 2 lead to a set of output phases corresponding to the majority gate truth table for all combinations of logical input signals. Animations of the magnetisation dynamics for selected combinations of input phases can be found in the supplementary information.

Figure 2 and the animations in the supplementary information show that spin waves do not only propagate towards the chosen output port position but also along the waveguide in the opposite direction. The inline spin wave majority gate in resonant operation conditions thus allows for a fan-out of two with only a small additional area of $4 F^2$ (total area $20 F^2$) and without the need to convert the spin wave signal back into the microwave domain. This is a highly desirable property for the design of more complex spin wave circuits. Adding additional output ports at other positions where the output waves are in phase can increase the fan-out even more. Inverting output ports are also possible at positions where the spin waves accumulate an additional phase shift of π . We note that the observed nonreciprocity of the spin wave intensity is a consequence of the chirality of the exciting magnetic field generated by the inductive antennas and can be avoided by using other types of spin waves, such as forward volume spin waves, or nonchiral spin wave transducers, *e.g.* magnetoelectric transducers [35]. However, as long as spin wave attenuation is small, the nonreciprocity does not affect device operation and fan-out.

All-electrical spin wave engineering. Building spintronic logic gates based on spin wave interference requires the quantitative assessment of the spin wave properties such as their dispersion relation and their propagation loss to allow for the control of both the amplitude and the phase of the spin waves at the output port. This can be achieved by a series of all-electrical two-port microwave measurements, in which spin waves are excited at an input port and, after propagation, analysed with phase sensitivity at the output port. The phase-sensitive spin wave transmission can then be inferred from the bias-field

derivative of the microwave S_{21} -parameter, dS_{21}/dH_{ext} , as shown in Fig. 3a for a 850-nm-wide $\text{Co}_{40}\text{Fe}_{40}\text{B}_{20}$ waveguide using P_3 as input and O as output port at a distance of 6.9 μm .

The shape of the transmitted signal can be understood as follows: during propagation over a distance r between input and output port, the spin wave phase rotates by a factor e^{ikr} , with $k = \frac{2\pi}{\lambda}$ being the spin wave wavevector. As a result, the real and imaginary parts of dS_{21}/dH_{ext} oscillate both in r and k . The correspondence between the wavevector k of the spin wave and its frequency f above the ferromagnetic resonance frequency—where k vanishes—is given by the spin wave dispersion relation. Spin waves attenuate during propagation because of the coupling between the magnetic degrees of freedom and the thermal bath, leading to a finite spin wave lifetime (typically 1 to 1.5 ns for permalloy and $\text{Co}_{40}\text{Fe}_{40}\text{B}_{20}$ waveguides in the studied frequency range) and hence a decay of the spin wave intensity with propagation distance. Typical spin wave group velocities in such waveguides in the studied frequency range are 5–10 $\mu\text{m}/\text{ns}$, resulting in decay lengths of the order of 10 μm , larger than characteristic propagation distances in the studied devices. The envelope of the frequency dependence of the spin wave response is determined mostly by the k -dependent coupling efficiency of the antennas. A one-dimensional model that takes into account the dispersion relation [36], the attenuation, and the antenna coupling efficiency is in excellent agreement with the experiment (see the supplementary information). The extracted spin wave dispersion relations for 850-nm-wide 30-nm-thick $\text{Co}_{40}\text{Fe}_{40}\text{B}_{20}$ waveguides at different magnetic bias fields are shown in Fig. 3b. At weak magnetic fields below the saturation of the magnetisation in the transverse direction (< 50 mT), contributions from backward-volume spin wave modes are also visible in the experimental data in Fig. 3a. However, these modes possess very short decay lengths and can therefore not be used for spin wave majority gate operation.

Electrical operation of nanoscale spin-wave majority gates. To design nanoscale spin wave majority gates, three different dimensions need to be considered: the waveguide width, the interport spacing, and the spin wave wavelength. We first consider an 850-nm-wide $\text{Co}_{40}\text{Fe}_{40}\text{B}_{20}$ waveguide with U-shaped antennas and an interport spacing of $2F = 2.3$ μm . Selecting a spin wave wavelength of $\lambda = 1.15$ μm , *i.e.* resonant conditions with $N = 2$, leads to higher spin wave excitation and detection efficiency by the U-shape antennas in this

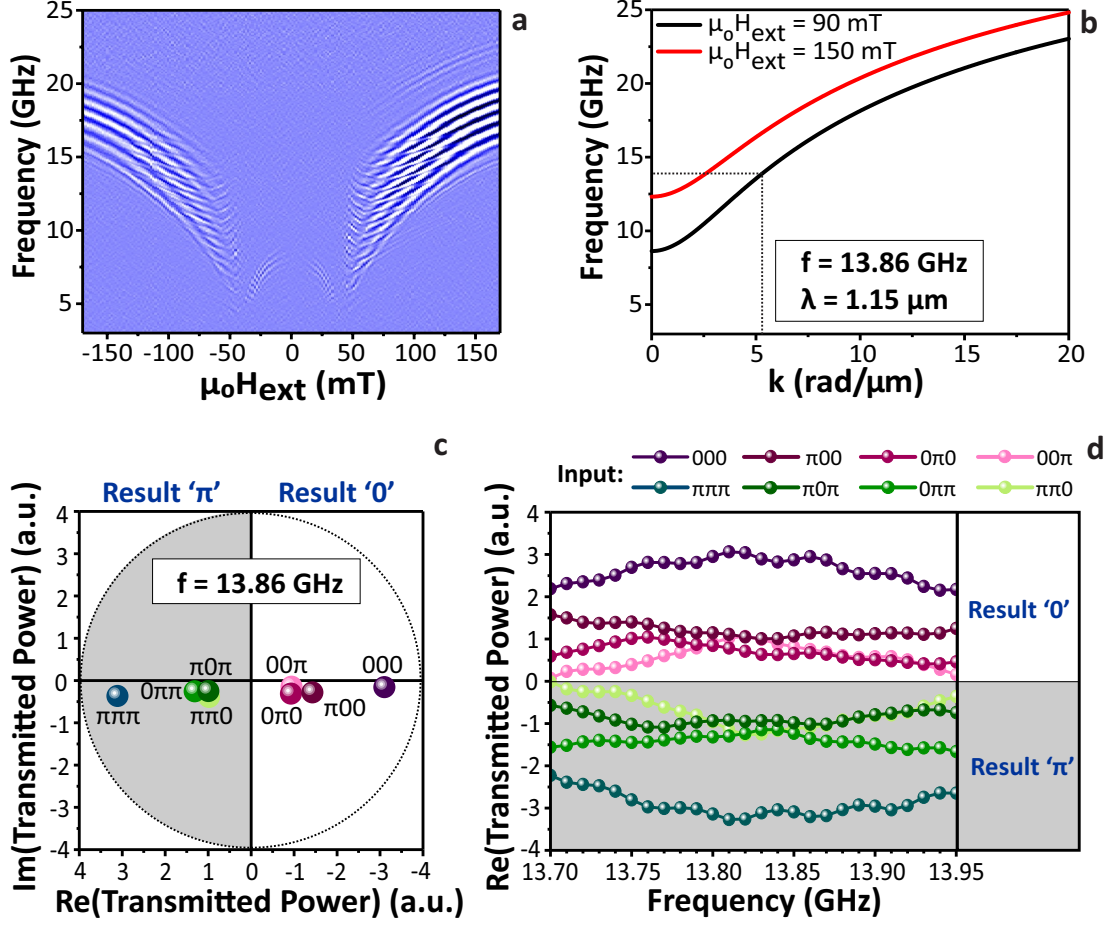


FIG. 3. **Spin wave dispersion and electrical operation of a nanoscale spin-wave majority gate.** **a)** Bias-field derivative of the imaginary part of the S_{21} microwave transmission parameter for spin wave propagation in a 850-nm-wide $\text{Co}_{40}\text{Fe}_{40}\text{B}_{20}$ waveguide between input P_3 and output O (distance of 6.9 μm) *vs.* frequency and transverse magnetic bias field. The oscillations stem from the phase accumulation during spin wave propagation. **b)** Dispersion relation of surface spin waves in a 850-nm-wide $\text{Co}_{40}\text{Fe}_{40}\text{B}_{20}$ waveguide for transverse magnetic bias fields as indicated. **c)** Complex polar plot of the transmitted power in a spin wave majority gate as a function of the input phases. Excitation frequency 13.86 GHz and magnetic bias field $\mu_0 H_{\text{ext}} = 90$ mT, *i.e.* resonant conditions with $N = 2$. Strong and weak majority signals can be clearly distinguished. **d)** Frequency-dependence of the real part of the transmitted power, indicating that the majority function can be obtained within an about 250-MHz-wide frequency band.

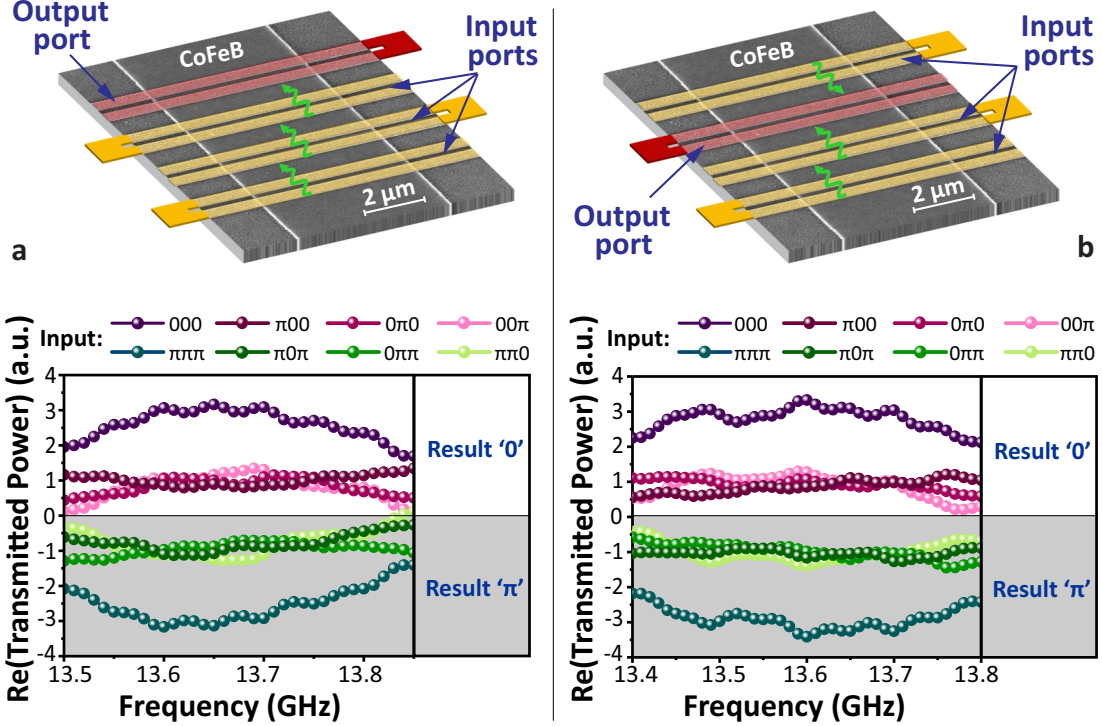


FIG. 4. **Reconfigurability of the spin-wave majority gate.** **a)** Configuration 1: schematic (top) and frequency-dependence of the real part of the transmitted power as a function of the three input phases in a spin wave majority gate using with a 4.7- μ m-wide $\text{Co}_{40}\text{Fe}_{40}\text{B}_{20}$ waveguide at a magnetic bias field of $\mu_0 H_{\text{ext}} = 42$ mT using an outer antenna as the output port. **b)** Configuration 2: experiment under identical conditions using an inner antenna as the output port. In both cases, the majority function of the input phases is found over an frequency window larger than 300 MHz.

wavelength range with respect to $N = 1$ and is therefore favourable. At the corresponding frequency of 13.86 GHz (at a transverse magnetic bias field of $\mu_0 H_{\text{ext}} = 90$ mT, see Fig. 3b), we explore all combinations of logical levels (input phases of 0 or π) and extract the phase at the output by analysing both the real and imaginary parts of the S_{21} -parameter (Fig. 3c) to successfully construct the full logic truth table of the majority function. All output states in this spin wave majority gate can be clearly distinguished within a frequency band of about 250 MHz around the target frequency (Fig. 3d). The clear separation between levels—including weak and strong majority cases—indicates that the device concept can be extended to n -input spin wave majority gates with $n > 3$ by adding additional input ports.

Reconfigurability of spin wave majority gates: ports as interchangeable inputs and outputs. Due to its symmetry, the inline spin wave majority gate can be used in a flexible way and any port can be chosen to be the output. Figure 4 illustrates two possible configurations: a first configuration with one of the outer antennas as the output port (Fig. 4a, as in all experiments described above), or an alternative second implementation when the output is one of the inner antennas (Fig. 4b). Using a 4.7- μm -wide $\text{Co}_{40}\text{Fe}_{40}\text{B}_{20}$ waveguide with an interport spacing of $2F = 2.3 \mu\text{m}$, the experimental spin wave transmission signals for these configurations (Fig. 4) demonstrate that the majority gate works equally well within a frequency band of more than 300 MHz when the roles of the ports are swapped. Similar to the case of fan-out discussed above, the behaviour is affected in this device design by the nonreciprocity of the surface spin waves and thus the spin wave intensities need to be adjusted when changing configurations. However, as mentioned before, such issues can be avoided by using other types of spin waves, such as forward volume spin waves, or nonchiral spin wave transducers.

Frequency-division multiplexing and operation at sub- μm wavelengths. The usage of waves for computation allows for frequency-division multiplexing and parallel computation in a majority gate with fixed geometry, enabling a larger computational throughout without additional area consumption. At low excitation powers, spin waves are noninteracting and different frequency channels can thus be used independently for logic operations. When nonresonant conditions are employed, spin wave majority gates can work at any frequency in the spin wave band above the ferromagnetic resonance, and the spacing of individual frequency subbands is only limited by the intrinsic line broadening due to the finite spin wave lifetime (about 100 to 150 MHz for the ferromagnetic materials chosen in this study). When resonant operation conditions with matched interport distances and spin wave wavelengths are chosen, frequency-division multiplexing can use a series of harmonics with $\lambda = \frac{2F}{N}$ and $N = 1, 2, 3, \dots$

The usage of different harmonics in a spin wave majority gate is illustrated by the calculated frequency dependence of the output signal (Fig. 5a) for all input phase combinations and the dispersion relation in Fig. 5b for a 4.7- μm -wide $\text{Co}_{40}\text{Fe}_{40}\text{B}_{20}$ waveguide and a magnetic bias field of $\mu_0 H_{\text{ext}} = 42 \text{ mT}$. For an interport spacing of $2.3 \mu\text{m}$, resonant operation of the spin wave majority gate with $N = 1$ and $N = 2$ is realised at frequencies around 12.2

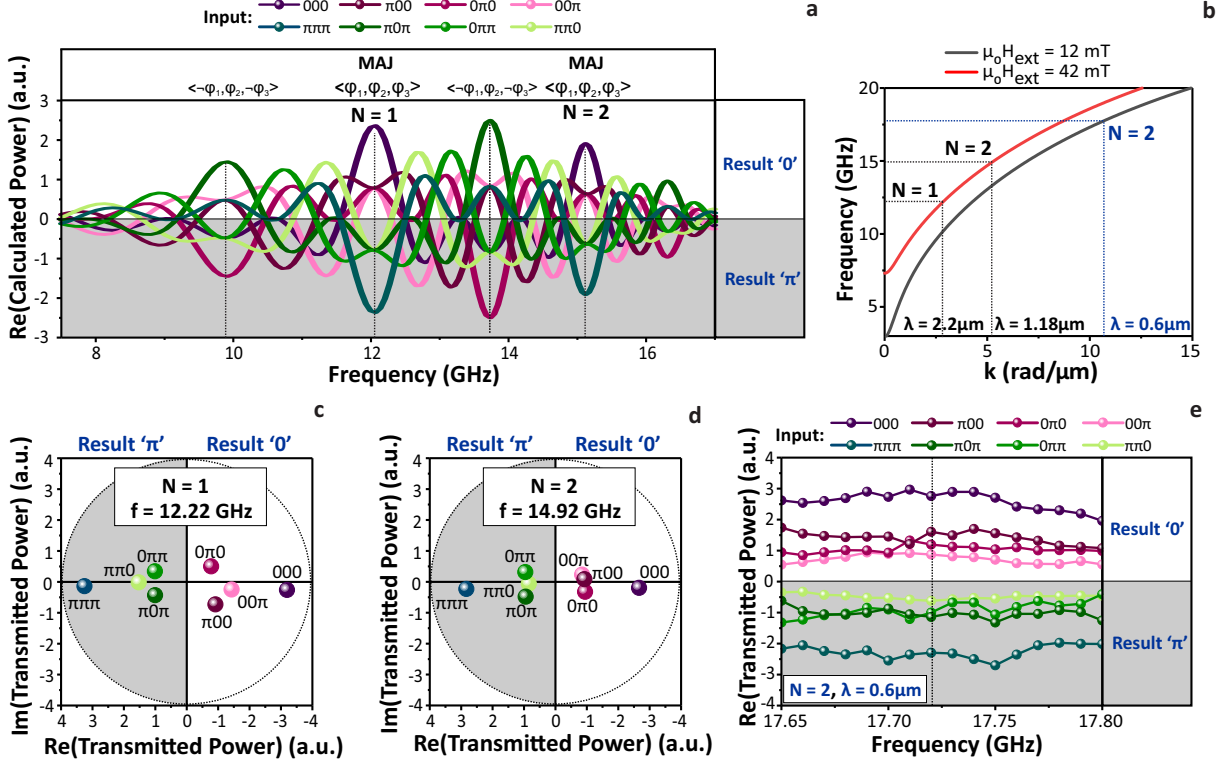


FIG. 5. Frequency-division multiplexing and operation at sub- μm wavelengths. **a)** Calculated real part of the output signal of a spin wave majority gate with a 4.7- μm -wide $\text{Co}_{40}\text{Fe}_{40}\text{B}_{20}$ waveguide, a magnetic bias field of $\mu_0 H_{\text{ext}} = 42$ mT, and an interport spacing of 2.3 μm . **b)** Corresponding dispersion relations of surface spin waves in the waveguide for magnetic bias fields as indicated. **c)** and **d)** Complex polar plots of the transmitted power in the spin wave majority gate at $\mu_0 H_{\text{ext}} = 42$ mT and frequencies of 12.22 GHz ($N = 1$) and 14.92 GHz ($N = 2$), respectively. At both frequencies, the full truth table of the majority function is obtained in the same device. **e)** Frequency-dependence of the real part of the transmitted power as a function of the input phases in a spin wave majority gate with a 4.7- μm -wide $\text{Co}_{40}\text{Fe}_{40}\text{B}_{20}$ waveguide, a magnetic bias field of $\mu_0 H_{\text{ext}} = 12$ mT, and an interport spacing of 1.2 μm . The majority function is obtained for a wavelength as low as 600 nm under resonant conditions with $N = 2$.

GHz and 15.1 GHz, respectively, as indicated in Fig. 5a. This behaviour is experimentally confirmed at frequencies of 12.22 GHz and 14.92 GHz, as shown in Figs. 5c and 5d, respectively. The experimental logic signals indicate that the majority function is obtained in the same device at these frequencies with $N = 1$ and $N = 2$, respectively. Additional higher harmonics with shorter wavelengths are outside the frequency range of the experimental

set-up. However, lowering the magnetic bias field to $\mu_0 H_{\text{ext}} = 12$ mT brings spin waves with sub- μm wavelengths into the accessible frequency range (Fig. 5b). Spin wave majority gate operation at a wavelength as low as 600 nm in a device using a 4.7- μm -wide $\text{Co}_{40}\text{Fe}_{40}\text{B}_{20}$ waveguide and an interport spacing of 1.2 μm is demonstrated in Fig. 5e at a frequency of 17.72 GHz for $N = 2$. The experimental logic signals allow for the deduction of the full majority function including a clear distinction between strong and weak majority.

Additional logic functions can also be implemented in the same device using different frequency bands. Using a wavelength of $\lambda = 4F$ leads to accumulated phases of the three spin waves upon propagation of π , 2π , and 3π , respectively, which implements the logic function $\text{MAJ}(\neg\varphi_1, \varphi_2, \neg\varphi_3)$, as illustrated in Fig. 5a at a frequency of 9.9 GHz. Note that the ports are still interchangeable and that “odd higher harmonics” ($\lambda = \frac{4F}{N}$ with $N = 1, 3, 5, \dots$) of this wavelength also provide the same logic function, as shown in Fig. 5a at 13.7 GHz for $N = 3$.

Parallel majority and minority (inverted majority, $\text{MIN} = \neg\text{MAJ}$) gate operation in a single device under resonant operation requires that the input and output ports are placed at positions $j \times 2F$, where $j = 1, 3, 5, 7$ are all odd integers, resulting in a larger area of at least $28 F^2$. Yet, parallel majority and minority gate operation in a $16 F^2$ minimum area spin wave majority gate is possible by taking advantage of the wave-based computing paradigm when the imaginary part of the signal—*i.e.* the signal that is shifted by $\frac{\pi}{2}$ with respect to the input reference phase of 0—is analysed. For resonant majority gate conditions, the imaginary part of the transmitted signal is always zero, as shown in Fig. 6a at frequencies of 12.2 GHz and 15.1 GHz for $N = 1$ and $N = 2$, respectively. At nearby frequencies, conditions exist, where the wavelength is such that the phase accumulation during the propagation between adjacent transducers (distance of $2F$) is $2\pi \times N \pm \frac{\pi}{4}$. As shown in Fig. 6a, the imaginary part of the output signal then leads to the minority (majority) function of the inputs at the corresponding frequency below (above) the resonant one. This is experimentally confirmed in a spin wave majority gate with a 4.7- μm -wide $\text{Co}_{40}\text{Fe}_{40}\text{B}_{20}$ waveguide, a magnetic bias field of $\mu_0 H_{\text{ext}} = 42$ mT, and an interport spacing of 2.3 μm for $N = 1$: operating the majority gate at 11.89 GHz ($\lambda = 2F / (1 - \frac{1}{8})$) and detecting the imaginary part of the transmitted power allows for the calculation of the minority function, as shown in Figs. 6b and 6c. By contrast, the operation at 12.53 GHz ($\lambda = 2F / (1 + \frac{1}{8})$) leads to the truth table

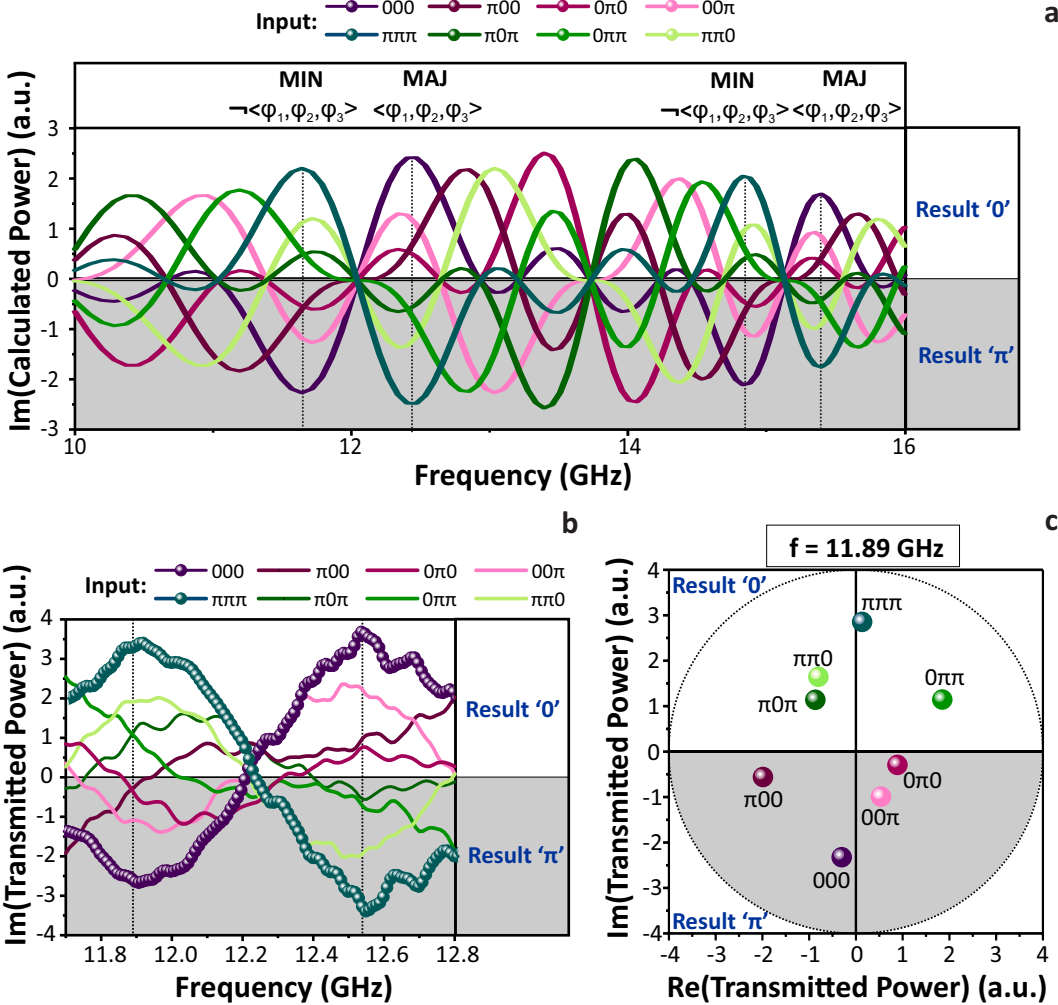


FIG. 6. **Variants of logic functions: minority gate.** **a)** Calculated imaginary part of the output signal of a spin wave majority gate with a 4.7- μ m-wide $\text{Co}_{40}\text{Fe}_{40}\text{B}_{20}$ waveguide, a magnetic bias field of $\mu_0 H_{\text{ext}} = 42$ mT, and an interport spacing of 2.3 μ m. Both MAJ and MIN ($= \neg \text{MAJ}$) functions are obtained in the same device. **b)** Experimental frequency dependence of the imaginary part of the transmitted power in the spin wave majority gate as a function of the input phases. MAJ and MIN logic functions are demonstrated at 12.53 GHz and 11.89 GHz, respectively. **c)** Complex polar plot of the transmitted power corresponding to minority gate operation at 11.89 GHz.

of the majority function (Fig. 6b). Again, higher harmonics can provide the same logic function and enable frequency-division multiplexing (Fig. 6a). These results show how the wave nature of the information carrier can be exploited to obtain parallel computation of identical or different logic functions in a single device.

Conclusion. These results demonstrate the robust operation of an inline spin wave majority gate using inductive microwave antennas as transducers between spin wave and electrical domains, and coding information in the phase of the spin waves. Imaging the magnetisation dynamics using time-resolved scanning transmission x-ray microscopy allowed for the reconstruction the full truth table of the majority function from the phase of the output wave with a clear distinction between strong and weak majority and a fan-out of two. All-electrical measurements using a vector-network analyser confirmed the behavior for sub- μm -wide waveguides and demonstrated that the intrinsic symmetry of the device allows for the reconfiguration of the device in the sense that any of the four ports can be chosen as the output.

The wave nature of the information carriers can be further exploited in several ways. Using different frequency bands allowed us to demonstrate frequency-division multiplexing in a single device, leading to improved throughput without increasing the area of the spin wave circuit. This allows for a flexible design of circuits with both frequency-division multiplexing capability and favourable dimensional scaling. Selecting proper operation frequencies enabled the calculation of different logic functions in the same device at different frequencies, including the parallel calculation of the majority and minority functions.

The results indicate that such inline majority gates are promising as the foundation of a future spin-wave-based ultralow-power superscalar vector computing platform. Achieving much lower computation power than current CMOS technology will require the usage of nonchiral spin wave transducers with higher energy efficiency, such as magnetoelectric transducers. In addition to applications in future spin wave computing technology, the generic devices can also be used to understand novel fundamental phenomena of spin waves in confined dimensions [37], including nonlinear interactions between different spin waves that occur at higher intensities. As the computing applications, such studies will greatly benefit from the flexibility as well as the scalability of the device design, including the ability to reach sub- μm waveguide sizes and spin wave wavelengths.

Supplementary information. Animations of the magnetisation dynamics in a spin wave majority gate with a 850-nm-wide $\text{Co}_{40}\text{Fe}_{40}\text{B}_{20}$ waveguide calculated by micromagnetic simulations for different combinations of input phases $[(\pi, \pi, \pi); (0, \pi, 0)]$. Animations of the experimental magnetisation dynamics in a spin wave majority gate with a 2- μm -wide

permalloy waveguide, imaged by time-resolved scanning transmission x-ray microscopy for different combinations of input phases $[(\pi, \pi, \pi); (\pi, 0, 0); (0, \pi, 0)]$. Detailed description of device processing as well as the all-electrical microwave measurement set-up. Details of inductive microwave antenna designs. Analytical model of spin wave transmission in all-electrical two-port experiments.

Author contributions. G.T, T.D, M.H., G.S., I.P.R., J.G., F.C., and C.A. conceived the experiments and designed the samples. G.T. fabricated the samples with device integration support from I.P.R and F.C. T.D. developed the experimental microwave set-up. G.T. and T.D. performed the microwave measurements. N.T., J.F., S.W., M.W., H.S., G.T., and J.G. performed the time-resolved scanning transmission x-ray microscopy measurements. G.T., T.D., F.C., and C.A. developed the dispersion models, confirmed by F.C. by micro-magnetic simulations. G.T., T.D., N.T., S.W., M.H., G.S., J.G., F.C., and C.A. analysed and interpreted the data. G.T., T.D., J.G., F.C., and C.A. prepared the manuscript. All authors commented on the manuscript.

Competing interests. The authors declare no competing interests.

Acknowledgements. This work has been supported by imec's industrial affiliate program on beyond-CMOS logic. It has also received funding from the European Union's Horizon 2020 research and innovation program within the FET-OPEN project CHIRON under grant agreement No. 801055. The authors would like to thank the Helmholtz-Zentrum Berlin (HZB) for the allocation of synchrotron radiation beamtime. Odysseas Zografos (imec) is acknowledged for designing a CMOS majority gate and determining its area.

Methods

Materials and devices. The devices consisted of ferromagnetic waveguides with widths between 850 nm and 4.7 μ m. Waveguide lengths were typically about 30 μ m, sufficiently long to avoid the influence of spin wave reflection at the waveguide ends on the device behaviour. Ta/Ni₈₀Fe₂₀/Ta (Ni₈₀Fe₂₀ = permalloy, 3 nm/30 nm/3 nm) waveguides were used for the scanning transmission x-ray microscopy measurements whereas Ta/Co₄₀Fe₄₀B₂₀/Ta (3 nm/30 nm/3 nm) was used in all-electrical microwave experiments. Spin waves were excited and detected by inductive antennas made from Al for scanning transmission x-ray microscopy and Au for microwave measurements, electrically connected to coplanar

microwave waveguides. Details of the sample fabrication can be found in the supplementary information. The saturation magnetisation of the films was determined by vibrating sample-magnetometry and was 0.8 MA/m and 1.36 MA/m for $\text{Ni}_{80}\text{Fe}_{20}$ and $\text{Co}_{40}\text{Fe}_{40}\text{B}_{20}$, respectively. Gilbert damping parameters were determined by ferromagnetic resonance measurements to be $\alpha = 7 \times 10^{-3}$ for $\text{Ta}/\text{Ni}_{80}\text{Fe}_{20}/\text{Ta}$ and $\alpha = 4 \times 10^{-3}$ for $\text{Ta}/\text{Co}_{40}\text{Fe}_{40}\text{B}_{20}/\text{Ta}$.

Time-resolved scanning transmission x-ray microscopy. Time-resolved scanning transmission x-ray microscopy measurements were carried out at the MAXYMUS end station at the UE46-PGM2 beamline at the Bessy II synchrotron within the Helmholtz-Zentrum Berlin. The samples were illuminated under perpendicular incidence by circularly polarised light in an external in-plane magnetic bias field of up to $\mu_0 H_{\text{ext}} = 240$ mT that was generated by a set of four rotatable permanent magnets [38]. The photon energy was set to the absorption maximum of the Fe L_3 edge to get optimal contrast for imaging. A lock-in-like detection scheme allowed for the measurement of the magnetisation dynamics—and in particular spin waves—excited at microwave frequencies with a time resolution of 50 ps using all photons emitted by the synchrotron. Input signals were provided by an arbitrary waveform generator, allowing for the independent control of both amplitude and phase of multiple microwave excitation channels. Further details on the detection and data analysis scheme can be found in [39].

All-electrical microwave measurements. Spin waves were both excited and detected using a vector network analyser (VNA). The three input antennas were connected to the single output channel of the VNA using two power dividers and variable attenuators to equalise the amplitudes of the microwave signals at each input port. To demonstrate the functionality of the spin wave majority gate, the relative phases at each port were then set by external delay-based phase shifters at the target frequency. The output antenna of the spin wave majority gate was connected to the receiver of the VNA. More details on the measurement system and the circuit behaviour can be found in the supplementary information.

Micromagnetic simulations. Micromagnetic simulations have been performed using the object-oriented micromagnetic framework (OOMMF) software package [40]. The geometry and the magnetic material parameters were chosen to correspond to experimental spin wave majority gates with $\text{Co}_{40}\text{Fe}_{40}\text{B}_{20}$ waveguides. The saturation magnetisation was assumed to be 1.36 MA/m, the exchange constant was 18.6 pJ/m, the Landé g factor was 2.07 [41], and the Gilbert damping was 4×10^{-3} . These parameters led to dispersion relations in excellent

agreement with the experiment as shown in the supplementary information.

* Email: christoph.adelmann@imec.be

- [1] Kajiwara, Y. *et al.* Transmission of electrical signals by spin-wave interconversion in a magnetic insulator. *Nature* **464**, 262–266 (2010).
- [2] Sander, D. *et al.* The 2017 magnetism roadmap. *J. Phys. D: Appl. Phys.* **50**, 363001 (2017).
- [3] Lenk, B., Ulrichs, H., Garbs, F. & Münzenberg, M. The building blocks of magnonics. *Phys. Rep.* **507**, 107–136 (2011).
- [4] Chumak, A.V., Vasyuchka, V.I., Serga, A.A. & Hillebrands, B. Magnon spintronics. *Nature Phys.* **11**, 453–461 (2015).
- [5] Cornelissen, L.J., Liu, J., Duine, R.A., Youssef, J.B. & van Wees, B.J. Long-distance transport of magnon spin information in a magnetic insulator at room temperature. *Nature Phys.* **11**, 1022–1026 (2015).
- [6] Haldar, A., Kumar, F. & Adeyeye, A.O. A reconfigurable waveguide for energy-efficient transmission and local manipulation of information in a nanomagnetic device. *Nature Nanotechnol.* **11**, 437–443 (2016).
- [7] Kim, J.-V., Stamps, R.L. & Camley, R.E. Spin wave power flow and caustics in ultrathin ferromagnets with the Dzyaloshinskii-Moriya interaction. *Phys. Rev. Lett.* **117**, 197204 (2016).
- [8] Wang, Q. *et al.* Reconfigurable nano-scale spin-wave directional coupler. *Sci. Adv.* **4**, e1701517 (2018).
- [9] Sluka, V. *et al.* Emission and propagation of 1D and 2D spin waves with nanoscale wavelengths in anisotropic spin textures. *Nature Nanotechnol.* **14**, 328–333 (2019).
- [10] Khitun, A. Multi-frequency magnonic logic circuits for parallel data processing. *J. Appl. Phys.* **111**, 054307 (2012).
- [11] Vogt, K. *et al.*, Realization of a spin-wave multiplexer. *Nature Commun.* **5**, 3727 (2014).
- [12] Awad, A.A. *et al.* Long-range mutual synchronization of spin Hall nano-oscillators. *Nature Phys.* **13**, 292–299 (2017).
- [13] Khitun, A., Nikonov, D.E. & Wang, K.L. Magnetoelectric spin wave amplifier for spin wave logic circuits. *J. Appl. Phys.* **106**, 123909 (2009).
- [14] Gladil, O. *et al.* Spin wave amplification using the spin Hall effect in permalloy/platinum

bilayers. *Appl. Phys. Lett.* **108**, 202407 (2016).

[15] Rovillain, P. *et al.* Electric-field control of spin waves at room temperature in multiferroic BiFeO₃. *Nature Mater.* **9**, 975–979 (2010).

[16] Chumak, A.V., Serga, A.A. & Hillebrands, B. Magnon transistor for all-magnon data processing. *Nature Commun.* **5**, 4700 (2014).

[17] Cornelissen, L.J., Liu, J., van Wees, B.J. & Duine, R.A. Spin-current-controlled modulation of the magnon spin conductance in a three-terminal magnon transistor. *Phys. Rev. Lett.* **120**, 097702 (2018).

[18] Hämäläinen, S.J., Madami, M., Qin, H., Gubbiotti, G. & van Dijken, S. Control of spin-wave transmission by a programmable domain wall. *Nature Commun.* **9**, 4853 (2018).

[19] Balinskiy, M. *et al.* Magnetoelectric spin wave modulator based on synthetic multiferroic structure. *Sci. Rep.* **8**, 10867 (2018).

[20] Khitun A. & Wang, K.L. Non-volatile magnonic logic circuits engineering. *J. Appl. Phys.* **110**, 034306 (2011).

[21] Radu, I.P. *et al.* Spintronic majority gates. *Proc. 2015 IEEE Intern. Electron Dev. Meet. (IEDM)*, 32.5 (2015).

[22] Zografos, O. *et al.* Non-volatile spin wave majority gate at the nanoscale. *AIP Adv.* **7**, 056020 (2017).

[23] Klingler, S. *et al.* Design of a spin-wave majority gate employing mode selection. *Appl. Phys. Lett.* **105**, 152410 (2014).

[24] Fischer, T. *et al.* Experimental prototype of a spin-wave majority gate. *Appl. Phys. Lett.* **110**, 152401 (2017).

[25] Sherazi, S.M.Y. *et al.* Standard-cell design architecture options below 5 nm node: the ultimate scaling of FinFET and nanosheet, *Proc. SPIE* **10962**, 1096202 (2019).

[26] Ciubotaru, F. *et al.* First experimental demonstration of a scalable linear majority gate based on spin waves, *Proc. 2018 IEEE Intern. Electron Dev. Meet. (IEDM)*, 36.1 (2018).

[27] Serga, A.A., Chumak, A.V. & Hillebrands, B. YIG magnonics. *J. Phys. D: Appl. Phys.* **43**, 264002 (2010).

[28] Madami, M. *et al.* Direct observation of a propagating spin wave induced by spin-transfer torque. *Nature Nanotechnol.* **6**, 635–638 (2011).

[29] Cherepov, S. *et al.* Electric-field-induced spin wave generation using multiferroic magnetoelec-

tric cells. *Appl. Phys. Lett.* **104**, 082403 (2014).

[30] Collet, M. *et al.* Generation of coherent spin-wave modes in yttrium iron garnet microdiscs by spin-orbit torque. *Nature Commun.* **7**, 10377 (2016).

[31] Talmelli, G. *et al.* Spin-wave emission by spin-orbit-torque antennas. *Phys. Rev. Appl.* **10**, 044060 (2018).

[32] Vlaminck, V. & Bailleul, M. Spin-wave transduction at the submicrometer scale: experiment and modeling. *Phys. Rev. B* **81**, 014425 (2010).

[33] Ciubotaru, F., Devolder, T., Manfrini, M., Adelmann, C. & Radu, I.P. All electrical propagating spin wave spectroscopy with broadband wavevector capability. *Appl. Phys. Lett.* **109**, 012403 (2016).

[34] Eshbach, J.R. & Damon, R.W. Surface magnetostatic modes and surface spin waves. *Phys. Rev.* **118**, 1208–1210 (1960).

[35] Duflou, R. *et al.* Micromagnetic simulations of magnetoelastic spin wave excitation in scaled magnetic waveguides. *Appl. Phys. Lett.* **111**, 192411 (2017).

[36] Kalinikos, B.A. & Slavin, A.N. Theory of dipole-exchange spin wave spectrum for ferromagnetic films with mixed exchange boundary conditions, *J. Phys. C: Solid State Phys.* **19**, 7013–7033 (1986).

[37] Demokritov, S.O. *Spin Wave Confinement: Propagating Waves* (2nd edition, Pan Stanford Publishing, Singapore, 2017).

[38] Nolle, D. *et al.* Note: unique characterization possibilities in the ultra high vacuum scanning transmission x-ray microscope (UHV-STXM) “MAXYMUS” using a rotatable permanent magnetic field up to 0.22 T. *Rev. Sci. Instrum.* **83**, 046112 (2012).

[39] Groß, F. *et al.* Nanoscale detection of spin wave deflection angles in permalloy. *Appl. Phys. Lett.* **114**, 012406 (2019).

[40] Donahue, M.J. & Porter, D.G. Interagency Report NISTIR 6376, National Institute of Standards and Technology, Gaithersburg, MD (1999).

[41] Liu, X., Zhang, W. Carter, M.J. & Xiao, G. Ferromagnetic resonance and damping properties of CoFeB thin films as free layers in MgO-based magnetic tunnel junctions. *J. Appl. Phys.* **110**, 033910 (2011).